

# Reaction dynamics study of $O^- + C_2H_2$ with crossed beams and density-functional theory calculations

Li Liu, Yue Li, and James M. Farrar<sup>a)</sup>*Department of Chemistry, University of Rochester, Rochester, New York 14627*

(Received 2 June 2005; accepted 24 June 2005; published online 7 September 2005)

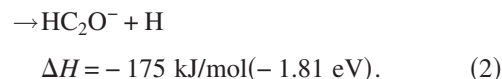
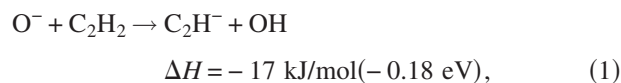
The reactions between  $O^-$  and  $C_2H_2$  have been studied using the crossed-beam technique and density-functional theory (DFT) calculations in the collision energy range from 0.35 to 1.5 eV (34–145 kJ/mol). Both proton transfer and C–O bond formation are observed. The proton transfer channel forming  $C_2H^-$  is the dominant pathway. The center-of-mass flux distributions of the  $C_2H^-$  product ions are highly asymmetric, with maxima close to the velocity and direction of the precursor acetylene beam, characteristic of direct reactions. The reaction quantitatively transforms the entire reaction exothermicity into internal excitation of the products, consistent with mixed energy release in which the proton is transferred in a configuration in which both the breaking and the forming bonds are extended. The C–O bond formation channel producing  $HC_2O^-$  displays a distinctive kinematic picture in which the product distribution switches from predominantly forward scattering with a weak backward peak to sideways scattering as the collision energy increases. At low collision energies, the reaction occurs through an intermediate that lives a significant fraction of a rotational period. The asymmetry in the distribution leads to a lifetime estimate of 600 fs, in reasonable agreement with DFT calculations showing that hydrogen-atom migration is rate limiting. At higher collision energies, the sideways-scattered products arise from repulsive energy release from a bent transition state. © 2005 American Institute of Physics. [DOI: 10.1063/1.2000947]

## I. INTRODUCTION

Negative-ion reactions play an important role in gas phase ion chemistry; a particularly timely topic that highlights such reactions is the emerging field of electron-initiated processes.<sup>1</sup> Understanding the formation mechanisms of negative ions and the reactions of such species in the context of the ion chemistry of planetary atmospheres, radiation chemistry, and combustion processes has motivated a number of studies.  $O^-$  is one of the most fundamental and important anions in gas phase chemistry, and studies of its reactions have been carried out since the beginning of negative-ion investigations.<sup>2,3</sup> The use of this species as a reactant in chemical ionization mass spectrometry<sup>4</sup> has placed significant emphasis on its reactions with hydrocarbons. A particularly interesting system is  $O^- + C_2H_2$ , which has been investigated with a variety of techniques at different ion energies in the past. The low-pressure ion source experiments of Neuert *et al.*<sup>5</sup> revealed two reaction channels. The product of proton transfer,  $C_2H^-$ , occurs approximately an order of magnitude more efficiently than the C–O bond formation process leading to the ketyl anion  $HC_2O^-$ . Stockdale *et al.*<sup>6</sup> have studied the products and rates in the ion energy range of 0–2 eV using a pulsed source mass spectrometer method. Parkes<sup>7</sup> measured the rate constants under near thermal energy conditions in a drift tube and determined that along with channels producing  $C_2H^-$ ,  $HCCO^-$ , and  $C_2^-$ , associative detachment (AD) to form  $H_2CCO + e^-$  accounted for 60% of the products. Futrell and Tiernan,<sup>8</sup> using a tandem

mass spectrometer, measured the total rate coefficient and the product branching ratio. Goode and Jennings<sup>9</sup> reported rate constants based on their ion cyclotron resonance investigations. Bohme *et al.*<sup>10</sup> studied the reaction at room temperature using the flowing afterglow method and determined the rate coefficient and branching ratio. Viggiano and Paulson<sup>11</sup> used the selected ion flow tube to measure the temperature dependence of the rate coefficient and branching ratio, using  $SF_6$  to scavenge electrons formed by AD. These studies were reviewed by Lee and Grabowski.<sup>4</sup> Most of these studies reported a product branching ratio for  $C_2H^-$  to  $HC_2O^-$  of about 8:1 at room temperature. More recently, the  $HC_2O^-$  anion has been studied by photodetachment spectroscopy<sup>12</sup> to yield the neutral ketyl radical, an important species in combustion.

The present work reports the first crossed-beam study of the  $O^- + C_2H_2$  reaction. There are two channels observed in our experiments:



We lack the capability to detect the electrons produced in the AD reaction. The signal from  $C_2^-$  products was below our detection limits. The proton transfer pathway is slightly exothermic, while the C–O bond formation process is highly exothermic. The enthalpy changes are determined from tabulated heats of formation of reactants and products.<sup>13</sup>

<sup>a)</sup>Author to whom correspondence should be addressed. Electronic mail: farrar@chem.rochester.edu

## II. EXPERIMENTAL METHOD

The experimental apparatus has been described previously,<sup>14</sup> so only a brief review is made here. O<sup>-</sup> ions are produced by electron impact on N<sub>2</sub>O (99.6%). The ions are accelerated to 300 V and are then mass selected with a 60° magnetic sector. After deceleration to the desired beam energy and focusing by a series of ion optics, the beam has an energy distribution with a full width at half maximum (FWHM) of ~0.17–0.22 eV. Experiments were performed at selected energies over a relative collision energy range of 0.35–1.52 eV. The acetylene gas (98%) is first passed through a cold trap to remove the acetone impurity. Then the beam is formed by supersonic expansion of the pure gas through a 0.07-mm nozzle. A 1.0-mm-diameter skimmer located 50 nozzle diameters downstream from the nozzle selects the cool core of the beam. Before entering the main chamber, the beam is collimated by passing through a 3.0-mm square aperture located approximately 2.5 cm from the skimmer in a differential pumping chamber. In the main chamber, the neutral beam intersects the ion beam at a 90° angle. A tuning fork chopper modulates the neutral beam at 30 Hz, allowing the separation of background from the true reactive scattering signal. An electrostatic energy analyzer with laboratory resolution of 0.07 eV is used to measure the kinetic energies of ions in the primary ion beam and scattered ionic reaction products. The resonant charge-transfer reaction between NO<sup>-</sup> and NO is used to determine the zero offset of the energy analyzer both before and after the reactive scattering measurements. The product ions are mass analyzed by a quadrupole mass spectrometer and detected by a dual microchannel plate ion detector. Data acquisition is computer controlled.

Two independent measurements were performed in the experiment. The kinetic-energy distributions of the scattered product ions were measured at several fixed laboratory angles. Each energy spectrum consists of 80 points, with typical energy bin widths of 0.025 eV. These kinetic-energy distributions were then normalized by measuring angular distributions of product ions in the laboratory coordinate system by summing up the signal over all energies. These data were corrected for drifting in the beams and detection efficiency by returning to a reference angle periodically and assuming that the drift in the signal is linear in time.

## III. DATA ANALYSIS

Dynamical interpretation of the experimental data is facilitated by transformation of the measured kinetic-energy and angular distributions of products to the center-of-mass (c.m.) coordinate system. The reactant beams in the experiments have velocity and angular spreads, resulting in distributions of collision energies and intersection angles. The laboratory flux at a particular scattering angle and velocity is expressed as an integral of the center-of-mass cross section over the beam velocity distributions and summed over final quantum states  $\{n\}$  according to the following equation:

$$I_{\text{lab}}(v, \Theta) = v^2 \int_0^\infty dv_2 f_2(v_2) \int_0^\infty dv_1 f_1(v_1) \frac{V_{\text{rel}}}{u^2} \times \sum_n I_{\text{c.m.}}(u_n, \theta; V_{\text{rel}}) \delta(u - u_n). \quad (3)$$

Inversion of this equation to the center-of-mass cross section is accomplished numerically on a grid via the following equation:<sup>15</sup>

$$I_{\text{lab}}(v, \Theta) = \sum_{i=1}^N f_i \frac{v^2}{u_i} I_{\text{c.m.}}(u_i, \theta_i). \quad (4)$$

In this expression,  $v$  and  $u_i$  are the product velocities in the laboratory and c.m. coordinates, respectively. The quantities  $f_i$  are the weighting factors for particular Newton diagrams with index  $i$  based on the reagent beam distributions. The extracted  $I_{\text{c.m.}}(u, \theta)$  can be transformed back to the laboratory frame, allowing comparison between the results of the deconvolution and the experimental data. Five points are used to represent the energy distributions of each of the two reagent beams, and five points represent the intersection angle distribution; thus, in the above equation,  $N$  is 125.

The barycentric angular distribution  $g(\theta)$  of the products can be calculated by integrating the derived  $I_{\text{c.m.}}(u, \theta)$  over product recoil speed.<sup>16</sup> The function  $g(\theta)$  represents the relative intensities of products scattered into c.m. scattering angle  $\theta$  averaged over product kinetic energy, evaluated by integration over c.m. speed  $u$ , as follows:

$$g(\theta) = \int_0^\infty I_{\text{c.m.}}(u, \theta) du. \quad (5)$$

Similarly, the angle-averaged relative translational energy distributions of products,  $P(E_T')$ , are calculated by integrating the c.m. intensity over the appropriate angular range as indicated by

$$P(E_T') = \int_0^\pi u^{-1} I_{\text{c.m.}}(u, \theta) \sin \theta d\theta. \quad (6)$$

The full flux distributions in velocity space as well as the kinetic-energy and angular distributions derived from them provide important physical insight into the nature of reactive collisions.

## IV. EXPERIMENTAL RESULTS

Cross sections for the proton transfer and C–O bond formation channels were measured at three different relative collision energies between 0.35 and 1.52 eV. The proton transfer reaction  $\text{O}^- + \text{C}_2\text{H}_2 \rightarrow \text{C}_2\text{H}^- + \text{OH}$  was studied at 0.35, 0.96, and 1.48 eV. The flux distributions in c.m. coordinates for the C<sub>2</sub>H<sup>-</sup> products were obtained by iterative deconvolution, as described previously. Figure 1 shows the flux distribution for the C<sub>2</sub>H<sup>-</sup> products at the lowest energy. The distributions at the higher collision energies are qualitatively similar to those in Fig. 1 and are not shown here. In the c.m. coordinate system, the directions of the O<sup>-</sup>-ion beam and the C<sub>2</sub>H<sub>2</sub> neutral beam are 0° and 180°, respectively.

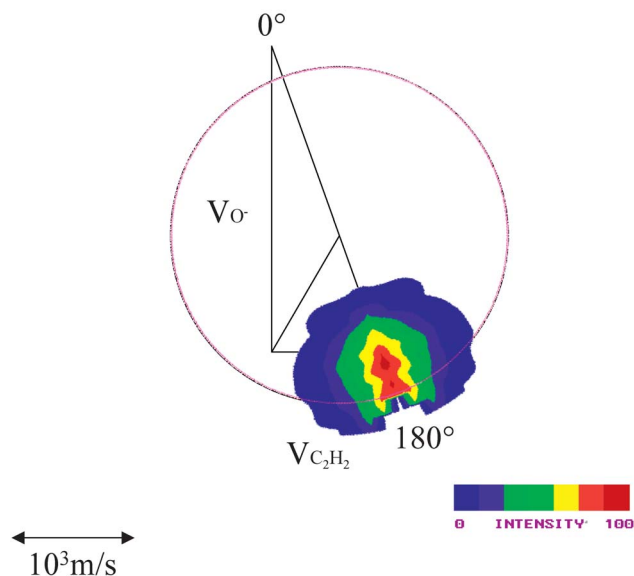
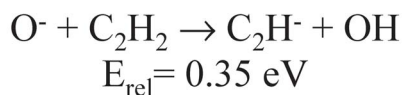


FIG. 1. (Color) Newton diagram and scattered  $C_2H^-$  product flux contour map at the collision energy of 0.35 eV.

The experimental results shown in the flux map indicate that the proton transfer flux distribution is sharply asymmetric, with the majority of the  $C_2H^-$  products scattered in the same direction as the precursor  $C_2H_2$  beam, with product velocities similar to the reagent neutral beam velocities. We denote this as forward scattering.<sup>17</sup> The observation of forward-scattered products indicates that the dominant proton transfer reaction mechanism is direct, proceeding through large impact-parameter collisions on a time scale much shorter than a rotational period of the transient association complex of the approaching reactants. This impulsive behavior is typical of dynamics of exothermic proton transfer reactions.

The angular distributions and relative translational energy distributions of the products of the proton transfer reaction at all three energies are shown in Fig. 2. The widths of the angular distributions show a slight narrowing with increasing collision energy, consistent with decreased interaction times at higher kinetic energies. In addition, there is a small, but perceptible peak in the backward direction at the lowest collision energy. Such scattering likely arises from small impact-parameter collisions. Figure 2(b) shows the relative translational energy distributions of the products at the three energies. As the collision energy increases, the relative translational energy distributions of the products shift towards higher energies; the widths of the distributions expressed as a fraction of the total available energy actually decrease.

The energy partitioning results are summarized in Table I. The total energy is the sum of collision energy, any reactant internal energy, and the reaction exothermicity. Reactant internal energy is negligible, as excited states of  $O^-$  undergo

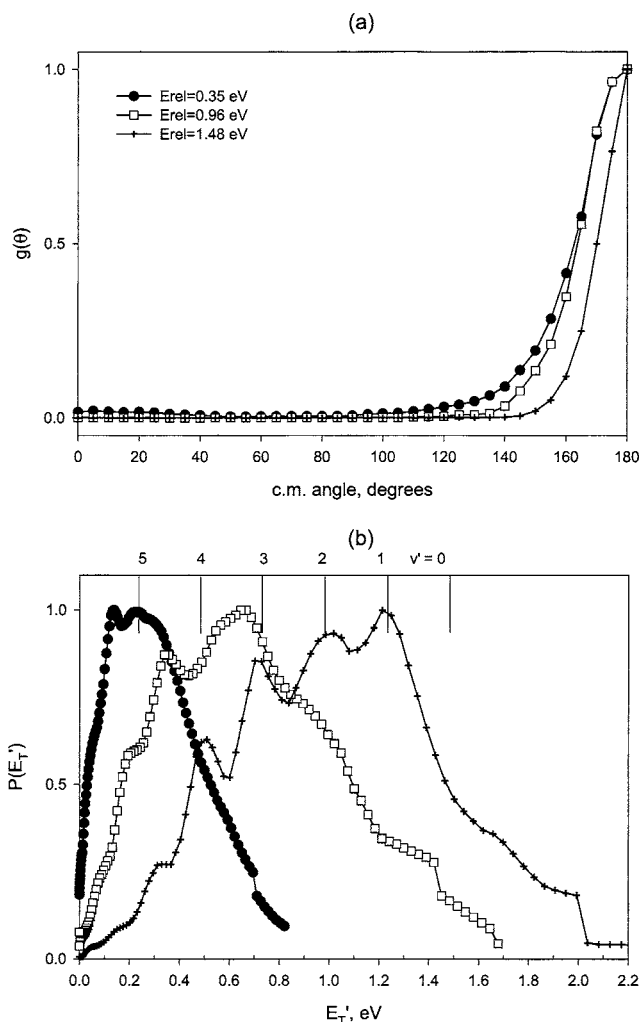


FIG. 2. (a) Angular distributions and (b) relative translational energy distributions for  $C_2H^-$  product in c.m. coordinate at all energies. The vertical tick marks correspond to translational energies of  $C_2H^-$  products formed in the 1.48-eV collision energy experiment with indicated numbers of quanta in the C-C stretch. Products have approximately 0.13 eV of rotational excitation.

rapid autodetachment, and the supersonic expansion produces internally cold neutral reactants. The product relative energy  $E_T'$  at each collision energy is tabulated as the average value of the appropriate relative translational energy distribution in Fig. 2(b). The data show a number of interesting trends. From conservation of energy, we determine that the fraction of the total energy appearing in product translation increases from 58% to 64% as the collision energy spans the full range studied here, demonstrating that an increased fraction of the incremental incident translational energy is trans-

TABLE I. Reaction energy partitioning results at different relative energies (in eV) for  $O^- + C_2H_2 \rightarrow OH + C_2H^-$ .

Reactant relative energy, $E_{rel}$	0.35	0.96	1.48
Total energy, $E_{total}$	0.53	1.14	1.66
Average product relative energy, $\langle E_T' \rangle$	0.31	0.71	1.06
$\langle E_T' \rangle / E_{total}$	0.58	0.62	0.64
Average product internal energy	0.21	0.43	0.60

TABLE II. Reaction energy partitioning results at different relative energies (in eV) for  $O^- + C_2H_2 \rightarrow H + HC_2O^-$ .

Reactant relative energy, $E_{rel}$	0.36	0.96	1.52
Total energy, $E_{total}$	2.17	2.77	3.33
Average product relative energy, $\langle E_T' \rangle$	1.27	0.91	1.35
$\langle E_T' \rangle / E_{total}$	0.59	0.33	0.41
Average product internal energy	0.90	1.86	1.98

formed into product translational energy. The average internal energy of the reaction products is 0.21 eV (20 kJ/mol) at the lowest collision energy, equal to the reaction exothermicity of 0.18 eV (17 kJ/mol) within experimental error. The average product internal excitation increases to 0.60 eV (58 kJ/mol) at the highest collision energy.

Measurements on the reaction channel  $O^- + C_2H_2 \rightarrow HC_2O^- + H$ , the C–O bond formation process, were obtained at 0.36, 0.96, and 1.52 eV (see Table II). Figures 3–5 are the polar flux distributions for  $HC_2O^-$  formation at these three energies. At the lowest energy, the distribution is asymmetric, with a sharp maximum near the precursor neutral beam, indicating forward scattering. The distribution also has a significant component of backward scattering, shown more clearly in the product angular distributions plotted in the top panel of Fig. 6. The possibility that this scattering is diagnostic of the participation of transient collision complexes living a significant fraction of a rotational period will be discussed later. As the collision energy increases, the product flux distribution changes considerably. At the intermediate collision energy, the distribution begins to spread through the entire velocity space accessible to the products. Along with

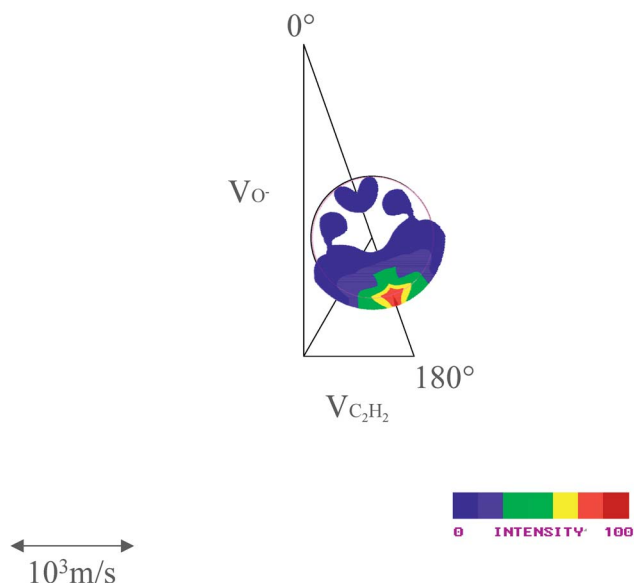
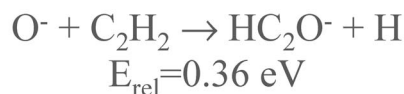


FIG. 3. (Color) Newton diagram and scattered  $HC_2O^-$  product flux contour map at the collision energy of 0.36 eV.

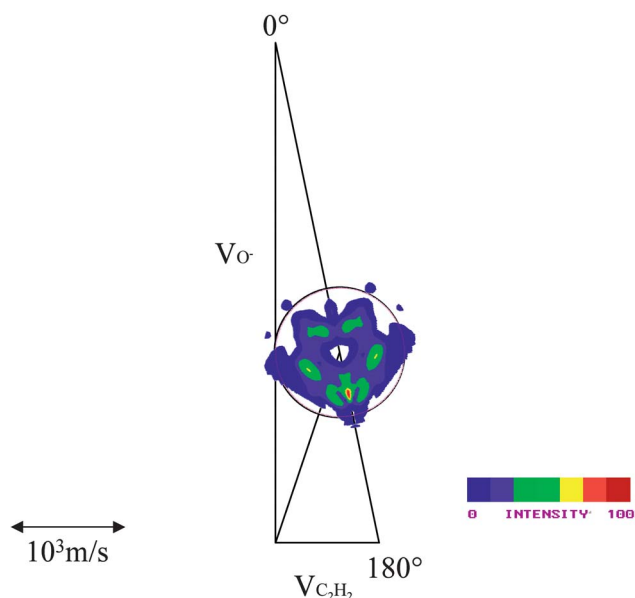
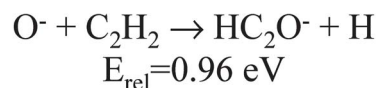


FIG. 4. (Color) Newton diagram and scattered  $HC_2O^-$  product flux contour map at the collision energy of 0.96 eV.

the local maximum at  $180^\circ$ , the distribution is broad throughout the entire sideways-scattered regime, with weak secondary maxima around  $100^\circ$  and  $35^\circ$ . At the highest energy, the forward-scattered peak is lost and the maximum occurs at

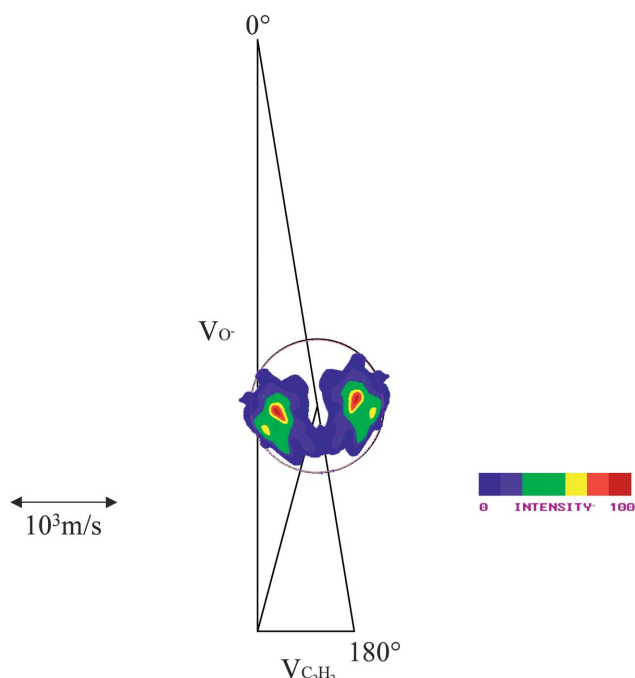
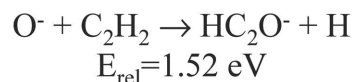


FIG. 5. (Color) Newton diagram and scattered  $HC_2O^-$  product flux contour map at the collision energy of 1.52 eV.

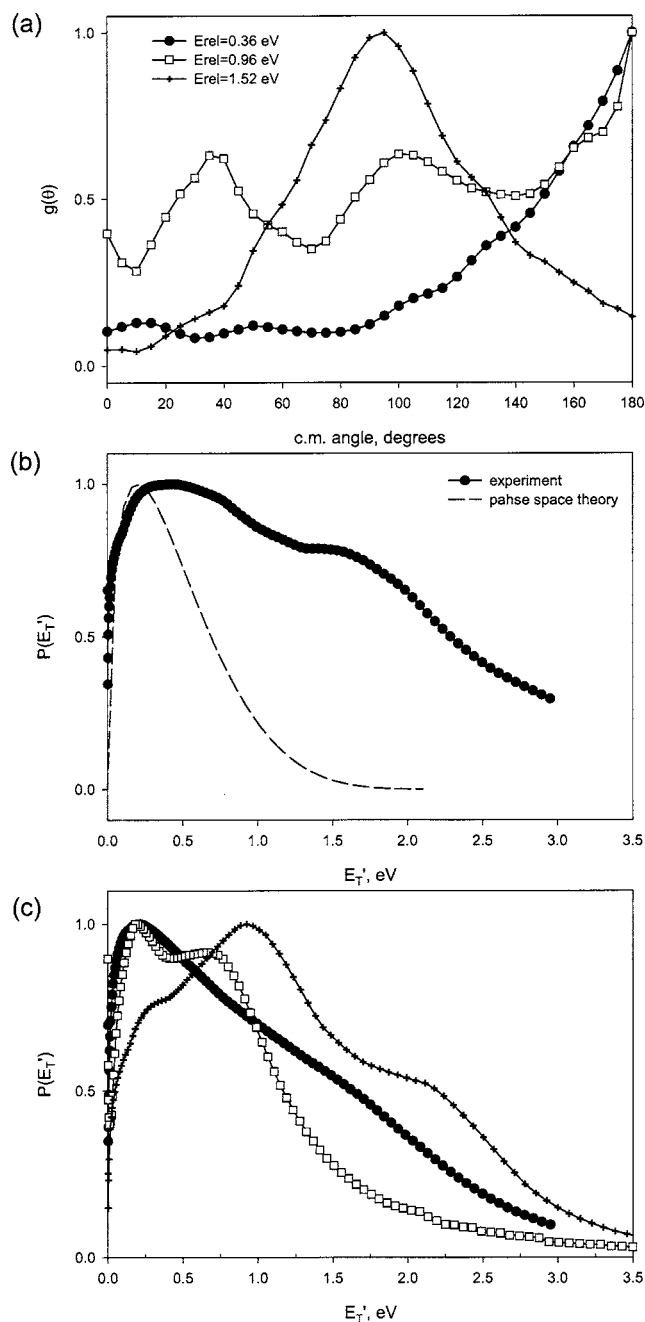


FIG. 6. (a) Angular distributions, (b) relative translational energy distribution for scattered  $HC_2O^-$  products in c.m. coordinates at the lowest collision energy, the dashed line shows the results of a statistical phase-space theory (PST) calculation, and (c) relative translational energy distributions for sideways-scattered  $HC_2O^-$  products. The distribution at  $0.36$  eV is computed by partial angular integration as described in the text.

approximately  $95^\circ$ . The comparison of the angular distributions in Fig. 6 illustrates clearly the shift from forward-backward scattering to sideways peaking. We will discuss the possible origin of such mechanism changes in a later section.

The middle panel of Fig. 6 shows the kinetic-energy distribution for the  $HC_2O^-$  products at the lowest collision energy. The distribution shows two broad peaks, the first of which occurs at  $\sim 0.5$  eV. A second broad maximum appears at  $\sim 1.5$  eV. Also shown in this panel is the result of a statistical phase-space theory (PST) calculation,<sup>18,19</sup> which agrees with the observed distribution in its rising edge, but is

significantly more narrow than the data. Although recent computational results by Troe *et al.*<sup>20</sup> suggest that anisotropies in the potential energy, which are ignored in the calculation presented in Fig. 6, may modify such PST kinetic-energy distributions significantly, the effects are expected to be small in the present system. In fact, the inclusion of such terms would shift the PST calculation to slightly higher energies, producing better agreement with experiment for the lower-energy feature in Fig. 6. Our purpose in comparing the kinetic-energy results with PST is to show that the high kinetic-energy products observed in the bimodal distribution of Fig. 6 do not likely arise from decay of a statistical complex, but from another mechanism discussed below.

The kinetic-energy distributions for the two highest-energy experiments are shown in the bottom panel of Fig. 6, along with the kinetic-energy distribution for the sideways-peaked products formed at the lowest collision energy. The rationale for plotting the distribution for the sideways-peaked products formed at  $0.36$  eV comes from the possibility that the lowest-energy data actually consist of a superposition of a complex-mediated mechanism and a direct mechanism proceeding through a bent transition state. The expected decrease in complex lifetime with increasing collision energy suppresses the transient complex contribution to the data at higher energies. The partial integration over the sideways-scattered products allows us to emphasize the direct contribution to the flux at the lowest energy. Qualitatively, the distributions do shift to higher kinetic energies with increasing collision energy, although the appearance of a high-energy tail shows that the partial angular integration does not completely separate the two components. A more complete discussion of the implications of these data is presented in Sec. VI that follows.

By measuring the intensities of the products of both channels, we estimate that the branching ratio of  $C_2H^-$  to  $HC_2O^-$  is about 4:1 to 3:1, decreasing as the collision energy increases. The dominance of direct proton transfer over the H-atom replacement is in accordance with other studies mentioned earlier in the paper.

## V. COMPUTATIONAL RESULTS

We performed density-functional theory (DFT) calculations with the GAUSSIAN98 program package<sup>21</sup> in order to elucidate structures of important reactive intermediates and the transition states connecting them. The geometries of all relevant species were fully optimized at the B3LYP/6-311+G\* level, and vibrational frequencies of important intermediates were then extracted in the harmonic approximation. Single point energy calculations were performed at the same level of theory based on the geometries and zero-point vibrational energies. For all open-shell species,  $\langle S^2 \rangle$ , the spin-squared expectation values, are close to the ideal value of 0.75 for spin eigenstates, indicating that spin contamination may be ignored. The energy levels of all species are shown in Fig. 7.

Five isomers for the  $[O \cdot C_2H_2]^-$  complex were obtained. Each reaction product also shows two stable isomers. The  $C_2H^-$  product of proton transfer has a linear isomer that lies

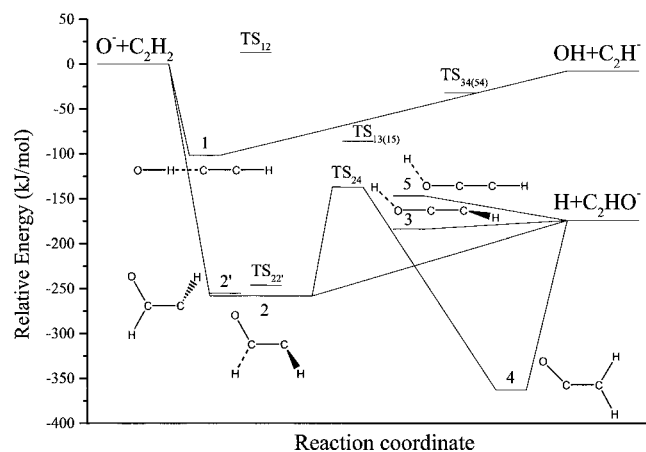


FIG. 7. Schematic reaction coordinate for  $O^- + C_2H_2$  reaction.

94 kJ/mol below the hydrogen-atom bridging isomer, denoted (b) in EPAPS.<sup>22</sup> The H-atom replacement product  $HC_2O^-$ , the ketenyl anion, is 237 kJ/mol more stable than the C-C-O-H structure, (b) in EPAPS. Figure 7 shows the structures of key intermediates; for clarity, the transition state structures are given via EPAPS. Our discussion will focus on the most stable reaction product isomers. The geometrical parameters, vibrational frequencies, and electronic energies for all intermediates, transition states, and products are accessible through EPAPS. The DFT results reported here for the  $HC_2O^-$  anion are in reasonable agreement with those reported by Schäfer-Bung *et al.*<sup>12</sup>

The DFT calculations show that the approaching reactants generate two different initial intermediates, depending on the details of the approach geometry. When the approaching  $O^-$  reactant interacts with a hydrogen atom on  $C_2H_2$ , intermediate 1 corresponding to a collinear hydrogen-bonded complex of nominal structure  $C_2H \cdots OH$ , is formed. This complex serves as direct precursor for the proton transfer product, decaying by simple bond cleavage without a barrier in excess of the reaction endothermicity.

When  $O^-$  approaches one of the carbon atoms of  $C_2H_2$  along a trajectory more nearly parallel to the perpendicular bisector of the C-C bond, an incipient C-O bond is formed, and  $sp \rightarrow sp^2$  rehybridization on the carbon occurs. Intermediates 2 and 2' correspond to complexes in which the hydrogen atoms are *cis* or *trans* to one another. The barrier between these *cis-trans* isomers is surprisingly low, only 9.1 kJ/mol, relative to complex 2' and 12 kJ/mol relative to complex 2. The C-C bond lengths in complexes 2 and 2' are 1.40 Å long,  $\sim 0.06$  Å longer than a typical C-C double bond, consistent with the low *cis-trans* barrier. Product formation may occur by hydrogen-atom loss from the carbon atom to which the incoming oxygen anion binds. As the incipient ketenyl radical anion forms, the C-C-O bending angle relaxes from  $\sim 133^\circ$  to nearly collinear. The C-H bond cleavage process occurs without a barrier in excess of the endothermicity.

Hydrogen-atom migration in intermediate 2/2' to create the ketene anion,  $H_2CCO^-$ , with both hydrogen atoms bound to the same carbon, denoted 4, may occur over a barrier of magnitude 120 kJ/mol. The migrating atom bridges the car-

bon atoms in the transition state for this process. The ketene anion 4 is approximately 105 kJ/mol more stable than intermediates 2/2'; this species also decays directly to reaction products with no barrier in excess of the endothermicity. The vibrational frequencies of intermediates and transition states calculated by DFT allow estimates of the relevant isomerization and decay rates and are discussed below.

Although structures 1 and 2/2', generated during collisions by different approach geometries, are distinct precursors to the products of proton transfer and C-O bond formation, respectively, the calculations also reveal that these pathways may be coupled by internal rotations occurring in intermediate 1. The calculations show that internal rotation of the OH moiety to form a species with an incipient C-O bond and a nearly linear C-C-O geometry, denoted species 3, has a barrier calculated to be only 16 kJ/mol. A structurally similar species 5 lies 37 kJ/mol above 3. In isomer 3, the O-H bond is 0.98 Å more extended than that in isomer 5 and the C-H bond forms  $145^\circ$  angle with the C-C bond instead of the almost linear structure of complex 5.

Complexes 3, 4, and 5 can decay directly to the  $HC_2O^-$  product; complexes 3 and 5 may also interconvert to the ketene anion, 4, by hydrogen-atom migration. Transition state  $TS_{34(54)}$  shown in Fig. 7 mediates this hydrogen-atom migration process. The calculations also show that the internal rotation of the OH unit may make the transition from isomer 1 to 2 possible. However, the transition state  $TS_{12}$  lies 115 kJ/mol above structure 1, even higher than the reactants. The high barrier suggests that this pathway does not play an important role in the reaction dynamics.

The DFT calculations allow us to evaluate vibrational frequencies for bound complexes and transition states, which can be used as input into rate constant calculations using Rice-Ramsperger-Kassel-Marcus (RRKM) statistical theory.<sup>23-26</sup> The standard RRKM formula is used to compute rates. The vibrational frequencies of complexes and relevant transition states that allow us to compute the appropriate sums and densities of states for the RRKM calculation are listed in the EPAPS data.<sup>22</sup> By examining the relative rate constants for direct dissociation in comparison with isomerization, we may discover additional constraints on reactive pathways.

We first consider the rate constants for direct decay of the initially formed complexes directly to their respective products. For decay of complex 1 to  $C_2H^-$  products, frequencies for the transition state were determined for structures in which the bond representing the reaction coordinate is extended to 4.0 Å. The calculations show that the rate of simple decay of complex 1 to the proton transfer product is approximately  $2 \times 10^{13} s^{-1}$ . This rate corresponds to a lifetime of 50 fs for complex 1, three orders of magnitude shorter than the rotational period of the complex estimated from moments of inertia extracted from the DFT calculations. The result is consistent with the direct dynamics we observe for this process.

The calculations also show that the decomposition of complex 2 to the  $HC_2O^-$  product occurs through a loose transition state with a rate of  $2 \times 10^{13} s^{-1}$ , which is substantially higher than the frequency of overall rotation of the

complex. Simply on the basis of the equal direct decay rates for complexes 1 and 2, the observed  $C_2H^-:HC_2O^-$  branching ratio, which lies between 3 and 4 at all energies, appears to reflect the dependences for the formation of the precursor complexes 1 and 2 on approach geometry. However, the observation that complex 2 exhibits an angular distribution at low collision energies with a measurable backward-scattered component indicates that the actual rate for the formation of  $HC_2O^-$  is significantly smaller than  $2 \times 10^{13} s^{-1}$ . We must therefore consider the role of isomerization processes in limiting the rates for product formation.

Considering the reactive pathways for complex 1 first, we calculate a rate constant for the  $1 \rightarrow 3/5$  isomerization process of  $2 \times 10^{13} s^{-1}$ . Complexes 3 and 5 decay directly to  $HC_2O^-$  with rates of  $2 \times 10^{14}$  and  $3 \times 10^{14} s^{-1}$ , respectively. The latter two complexes may also isomerize to the ketene anion 4, which then forms  $HC_2O^-$ , but the calculated rates for the  $3/5 \rightarrow 4$  processes, in the range of  $10^{10}$ – $10^{11} s^{-1}$ , are too small to be competitive. Thus, statistical theory predicts that complex 1 decays to both reaction products with equal rates. Both the observed branching ratio and the angular distribution evidence for a transient intermediate living a significant fraction of a rotational period for  $HC_2O^-$  formation, but not for  $C_2H^-$  production, argue against this interpretation.

In fact, it is more reasonable to consider the formation of  $C_2H^-$  via proton transfer as a direct reaction; the RRKM calculations simply reveal that the predicted lifetime of intermediate 1 is too short to support a transient intermediate that lives a significant fraction of a rotational period. In this sense, the observed dynamics and RRKM theory are compatible.

We gain more insight into the pathway for forming  $HC_2O^-$  by considering isomerization pathways that follow the formation of complex 2. As we have already noted, DFT calculations indicate that the barrier for hydrogen-atom migration in complex 2 to form the ketene anion 4 lies below the energy of the approaching reactants, and RRKM calculations show that the rate of  $2 \rightarrow 4$  isomerization is  $3 \times 10^{12} s^{-1}$ ; subsequent decay of 4 to  $HC_2O^-$  products is very fast, occurring with a rate  $> 10^{14} s^{-1}$ . Thus, the DFT/RRKM calculations suggest that the rate limiting step for  $HC_2O^-$  formation from complex 2 is  $3 \times 10^{12} s^{-1}$ . The characteristic frequency for this isomerization is  $\sim 300$  fs, of comparable magnitude to rotational periods of polyatomic molecules. In Sec. VI, we will discuss the consistency of this observation with the experimental data.

## VI. DISCUSSION

The experimental data and DFT calculations suggest that the product branching is governed primarily by approach geometry, reflected in the relative orientations of approaching reactants. When  $O^-$  approaches  $C_2H_2$  along a trajectory that proceeds through a nearly collinear  $O \cdots H-C$  geometry, complex 1 will be formed and proton transfer will occur. If  $O^-$  approach either carbon atom, complex 2 will be formed, leading to C–O bond formation.

Rate constant data described previously indicate that AD is the dominant reaction at thermal energies. The prototype systems  $OH^-$  (Ref. 27) and  $H_2O^-$  (Ref. 28) indicate that AD in such systems occurs as a result of specific electronic-vibrational interactions. In the case of  $H_2O^-$ , the bending vibration is coupled to the detachment coordinate. In the  $[H_2CCO]^-$  system, there may be several vibrational modes of complexes 1 or 2/2' that lead to electron detachment rather than proceeding to the products we have observed. Thus, information on the specific geometries that lead to  $C_2H^-$  or  $HCCO^-$  products may be indicative of motions that are not involved in electron detachment. The DFT calculations presented above and the experimental data do not allow us to determine if the ketene molecule is formed as a result of isomerization on the anionic surface, followed by detachment, or by fast detachment followed by isomerization on the neutral surface. In addition, determining the coupling strengths of bound-continuum interactions leading to AD and the ranges of geometries over which those couplings operate are beyond the scope of the DFT calculations reported here.

The proton transfer process forming  $C_2H^-$  exhibits many of the characteristics of direct reactions that we have studied recently in this laboratory.<sup>17,29,30</sup> This proton transfer reaction is an example of a heavy+light–heavy system in which a light particle, H, is transferred between heavier molecular fragments. The potential-energy surface for this transfer, expressed in the scaled and skewed coordinates that allow the Hamiltonian to be expressed in a diagonal quadratic form,<sup>31</sup> is characterized by a very acute angle,  $18^\circ$  for this system, between the entrance and exit channels. The classic energy disposal motif for this mass combination is “mixed energy release”<sup>32–35</sup> in which reaction occurs with the cleaving and incipient bonds in extended configurations.

Reactive collisions on such highly skewed surfaces are direct, with a strong propensity to cut the corner separating the entrance and exit valleys. These motions correspond to light atom transfer from configurations extended from equilibrium bond lengths with little momentum transfer to the departing heavy atoms and yield vibrationally excited reaction products. In the study reported here, the exothermicity of the proton transfer reaction,  $-0.18$  eV, is relatively small in comparison with the range of collision energies (0.35–1.48 eV). At the lowest collision energy, the average value of the product internal energy is 0.26 eV, indicating that the entire reaction exothermicity and a small fraction ( $\sim 23\%$ ) of the relative translational energy appears in the internal excitation of the products. The quantitative transformation of the entire reaction exothermicity into internal excitation is consistent with an early release of the exothermicity with the nascent bond extended from its equilibrium configuration, as expected for mixed energy release. Precisely this motif has been observed in the previous studies of proton transfer reactions reported from this laboratory. However, in those systems, the substantially higher exothermicities yield much higher fractions of available energy in internal excitation of the products.

The energy partitioning observed at the lowest collision energy provides a base line for evaluating the role of incremental translational energy. Experimental data at higher col-

lision energies provide insight into the reaction dynamics along two different lines of thought. First, we note that the product kinetic-energy distributions shown in the lower panel of Fig. 2 exhibit a steady shift to higher energies with increasing collision energy. At the lowest collision energy, 58% of the available energy appears in product translation; the *incremental* translational energies associated with the two higher-energy experiments are disposed in the products with slightly more selectivity. At the intermediate collision energy of 0.96 eV, 64% of the incremental translational energy appears in product translation; at the highest collision energy of 1.48 eV, a slightly increased fraction, 68% of the increment partitions in product translation. The small skew angle of the reduced dimensionality surface that describes collinear proton transfer provides an explanation for the transformation of incremental translational energy into product translation. The concept of “induced repulsive energy release” was introduced to address partitioning of incremental translational energy on heavy+light-heavy potential surfaces.<sup>36</sup> In this picture, reactive trajectories with excess translation penetrate far into the “corner” of the highly skewed potential surface where both the forming and breaking bonds are compressed. The trajectory moves into the exit valley with little motion perpendicular to the reaction coordinate, yielding products with high translational excitation.

In the present system, the effect of such “induced” repulsive energy release is significantly weaker than we have observed in other systems. For example, in the  $\text{H}_3\text{O}^+ + \text{NH}_3$  system,  $\sim 30\%$  of the available energy appears in product translation at the lowest collision energy, but at higher collision energies, essentially 100% of the incremental translation is transformed into product translation. In its most simple form, induced repulsive energy release does not take into account the internal structures of the molecular fragments between which the light particle occurs. The experimental data for the present system at higher collision energies provide direct evidence that internal degrees of freedom of product fragments do, in fact, carry significant excitation. The product kinetic-energy distributions at the two highest collision energies, shown in Fig. 2(b), exhibit oscillatory structure with regular spacings of 0.20–0.25 eV. Using DFT calculations for  $\text{C}_2\text{H}^-$  and published molecular constants for OH,<sup>37</sup> it is relatively straightforward to assign these spacings to C–C stretching excitation in  $\text{C}_2\text{H}^-$  ( $1907\text{ cm}^{-1}$ , 0.24 eV). Vibrational frequencies associated with C–H or O–H stretching motions occur at measurably higher energies, in the range from  $3000$  to  $3500\text{ cm}^{-1}$ , or 0.37–0.43 eV. The vertical lines in the plot of the translational energy distributions in Fig. 2(b) correspond to the kinetic energies of rotationally cold species in which the products formed at 1.48-eV collision energy have a specified number of quanta in C–C stretching modes. Rotational excitation in either fragment accounts for the shifts in the observed peak positions relative to the calculated positions. It is interesting to note that according to the DFT calculations, the C–C bond lengths change only  $\sim 0.04\text{ \AA}$  as reactants approach, pass through complex 1 and associated transition states, and evolve to products. Despite this relatively small change, significant excitation is observed in this coordinate.

The C–O bond formation channel also exhibits an interesting dynamical signature with significant energy dependence. At the lowest energy, the reactive flux shows a strong forward peak, but with a significant component of backward-scattered products. Complex 2 has near-prolate symmetric top character ( $A \approx 100\text{ GHz}$ ;  $B \approx C \approx 10\text{ GHz}$ ), and the decay of such a complex along its principal symmetry axis produces angular distributions with peaks at  $0^\circ$  and  $180^\circ$ .<sup>38</sup> The asymmetry in the angular distribution permits an estimate of the collision complex lifetime within the “osculating model” for chemical reactions<sup>39–41</sup> proceeding through complexes that live a fraction of a rotational period. This model parametrizes the forward-backward asymmetry in the angular distribution in terms of the ratio of the complex lifetime  $\tau$  to its rotational period  $\tau_R$  as follows:

$$g(\pi)/g(0) = \cosh(\tau_R/2\tau). \quad (7)$$

The angular distribution at the lowest collision energy, shown in Fig. 6, suggests that the forward-backward intensity ratio is about 7 and thus  $\tau_R/\tau \approx 5$ . Rate constant data<sup>9</sup> provide an estimate of the maximum impact parameter for complex formation, leading to a value of  $30\hbar$  for the total angular momentum. The  $B, C$  rotational constant from DFT calculations for complex 2/2' is  $\sim 10\text{ GHz}$ . These values result in a rotational period for complex 2 of  $\sim 3\text{ ps}$  and a corresponding lifetime of  $\sim 600\text{ fs}$ . This result is in reasonable agreement, within a factor of 2, with the RRKM lifetime inferred from the rate of isomerization through  $\text{TS}_{24,3}$   $\times 10^{12}\text{ s}^{-1}$ .

At the higher collision energies, most vestiges of transient complex decay have vanished, and the angular distributions provide information about preferred geometry of the transition state leading to hydrogen-atom emission. At the highest collision energy of these studies, 1.5 eV, the angular distribution for product formation shows a very strong sideways peak near  $100^\circ$ ; at this collision energy, the system passes through the region of the potential surface near complex 2 on a time scale sufficiently rapid that direct decay to products is strongly favored over any isomerization bottlenecks. Configurations resembling complex 2, in which the cleaving C–H bond makes angles near  $110^\circ$  with respect to the axis of the C–C bond, and thus with the direction of the nascent C–O bond in the ketylenyl anion, appear to dominate the dynamics. The sideways peaking is the result of a direct decay governed by a bent transition state, very similar to that exhibited for the  $\text{H} + \text{Br}_2$  system.<sup>42</sup>

The kinetic-energy distributions associated with the formation of  $\text{HC}_2\text{O}^-$  are also revealing of the dynamics. At the lowest collision energy, where the rotational period of the intermediate complex serves as a “clock” for the decay process, the system appears to proceed through the transition state of the  $2 \rightarrow 4$  hydrogen-atom migration process. Interestingly, the product kinetic-energy distribution shown in Fig. 6 is anomalously broad and shows evidence for two features. The low-energy feature has a weak peak that is qualitatively in accordance with what one would expect for decay of a transient complex living a significant fraction of a rotational period. Agreement between this feature of the kinetic-energy distribution and the phase-space theory calculation<sup>18,19</sup> is not

particularly good, suggesting that the decay is not statistical. The higher-energy feature, peaking near 1.8 eV, indicates that a significant fraction of the reaction products is formed with substantial kinetic energy. Examination of the details of the double-minimum potential surface<sup>43,44</sup> proposed to explain the observed rate of production of  $HC_2O^-$  provides insight into the origin of these translationally excited products. The decay rate for complex 4 has been calculated to be  $>10^{14} s^{-1}$ . Almost certainly, this time scale is too short for statistical reequilibration of the internal energy of the system following passage over the isomerization barrier. Thus, the isomerization barrier behaves like an exit channel barrier, exhibiting the characteristic repulsion that forms products with high translational energy. That is, the products pass through regions of the potential surface in the vicinity of complex 4 far too quickly to redistribute energy among the vibrations of this species.

At higher collision energies, the product angular distributions develop a strong sideways-peaked feature and the corresponding kinetic-energy distributions peak at lower energies than observed when the system exhibits the forward-backward peaking characteristic of a transient complex. In order to see whether the broad flux distribution exhibited by the reaction products at the lowest collision energy also has a small contribution from direct collisions proceeding through a bent transition state, we have calculated product kinetic-energy distributions separately for the forward, sideways, and backward-scattered products. These partially angularly averaged kinetic-energy distributions are calculated by replacing the limits of integration in Eq. (6) with the values  $(2\pi/3, \pi)$ ,  $(\pi/3, 2\pi/3)$ , and  $(0, \pi/3)$ , respectively. The results of this calculation are plotted in the third panel of Fig. 6, and show clearly that the kinetic-energy distributions for the forward-backward products are broad, consistent with the contribution from the kinetic-energy release associated with descending from the isomerization barrier, while the sideways-scattered product distribution peaks at low energies. A comparison of the kinetic-energy distributions for these sideways-scattered peaks at all three collision energies shows a monotonic increase in  $\langle E_T' \rangle$  with collision energy. This analysis shows clearly that the mechanism for  $HC_2O^-$  formation evolves from a superposition of complex (forward-backward) and direct (sideways) components at low energies to an impulsive process in which the product angular distributions reflect the bent transition state geometry quite clearly.

The kinetic-energy distributions for  $HC_2O^-$  formation via the bent transition state tend to peak at kinetic energies  $\leq 1$  eV, corresponding to products with 1–2 eV of internal excitation. On the basis of the geometry changes that occur as configurations like complex 2 evolve to products, we predict substantial levels of internal excitation in the products. The significant change in the C–C–O bond angle in going from complex 2 to products ( $129^\circ$ – $180^\circ$ ), and the 0.14 Å decrease in the C–C bond length suggest that the corresponding bending and stretching modes in the products will be substantially excited.

## VII. CONCLUSIONS

The reactions of  $O^-$  with  $C_2H_2$  to form  $C_2H^-$  and  $HCCO^-$  exhibit a number of dynamical features that have been interpreted with the assistance of DFT calculations. The proton transfer reaction shows characteristics of both mixed energy release and induced repulsive energy release typical of the energy dependence of the dynamics associated with the heavy+light-heavy mass combination. However, excitation of the C–C stretching vibration in the  $C_2H^-$  products demonstrates that the internal structure of the heavy fragments also plays a critical role in the dynamics. The C–O bond formation channel is especially interesting. At low energies, the system exhibits clear evidence for the participation of a transient complex living a fraction of a rotational period. The DFT calculations suggest that the rate of product formation is limited by the rate of hydrogen-atom migration. Moreover, the product kinetic-energy distributions show clear evidence for large kinetic-energy release associated with descent from the barrier associated with this isomerization. With increasing collision energy, the complex lifetime is too short to influence the energy and angular distributions of the products, and the angular distributions present direct evidence for the role of a bent transition state. Neither the DFT calculations nor the experimental data allow us to draw any specific conclusions concerning the dynamics of the AD process.

The synergy between experiment and theory suggests that the concepts revealed by these relatively simple systems will provide a foundation for studies on more complex systems. We also hope that the present work will inspire detailed dynamical calculations to confirm and extend the conclusions presented here. We look forward to those additional developments.

- <sup>1</sup>B. C. Garrett, D. A. Dixon, D. M. Camaioni *et al.*, Chem. Rev. (Washington, D.C.) **105**, 355 (2005).
- <sup>2</sup>F. C. Fehsenfeld, E. E. Ferguson, and A. L. Schmeltekopf, J. Chem. Phys. **45**, 1844 (1966).
- <sup>3</sup>F. C. Fehsenfeld, A. L. Schmeltekopf, H. I. Schiff, and E. E. Ferguson, Planet. Space Sci. **15**, 373 (1967).
- <sup>4</sup>J. Lee and J. J. Grabowski, Chem. Rev. (Washington, D.C.) **92**, 1611 (1992).
- <sup>5</sup>H. Neuert, R. Rackwitz, and D. Vogt, Adv. Mass Spectrom. **4**, 631 (1968).
- <sup>6</sup>J. A. D. Stockdale, R. N. Compton, and P. W. Reinhardt, Int. J. Mass Spectrom. Ion Phys. **4**, 401 (1970).
- <sup>7</sup>D. A. Parkes, J. Chem. Soc., Faraday Trans. 1 **68**, 613 (1972).
- <sup>8</sup>J. H. Futrell and T. O. Tiernan, in *Ion-Molecule Reactions*, edited by J. L. Franklin (Plenum, New York, 1972), Vol. 2, Chap. 11.
- <sup>9</sup>G. C. Goode and K. R. Jennings, Adv. Mass Spectrom. **6**, 797 (1974).
- <sup>10</sup>D. K. Bohme, G. I. Mackay, H. I. Schiff, and R. S. Hemsworth, J. Chem. Phys. **61**, 2175 (1974).
- <sup>11</sup>A. A. Viggiano and J. F. Paulson, J. Chem. Phys. **79**, 2241 (1983).
- <sup>12</sup>B. Schaefer-Bung, B. Engels, T. R. Taylor, D. M. Neumark, P. Botschwina, and M. Peric', J. Chem. Phys. **115**, 1777 (2001).
- <sup>13</sup>NIST, <http://webbook.nist.gov/chemistry/>, 2003.
- <sup>14</sup>D. F. Varley, D. J. Levandier, and J. M. Farrar, J. Chem. Phys. **96**, 8806 (1992).
- <sup>15</sup>P. E. Siska, J. Chem. Phys. **59**, 6052 (1973).
- <sup>16</sup>Z. Herman, Int. J. Mass. Spectrom. **212**, 413 (2001).
- <sup>17</sup>L. Liu, X. Cai, Y. Li, E. R. O'Grady, and J. M. Farrar, J. Chem. Phys. **121**, 3495 (2004).
- <sup>18</sup>P. Pechukas, J. C. Light, and C. Rankin, J. Chem. Phys. **44**, 794 (1966).
- <sup>19</sup>W. J. Chesnavich and M. T. Bowers, J. Chem. Phys. **66**, 2306 (1977).

- <sup>20</sup>J. Troe, V. G. Ushakov, and A. A. Viggiano, *Z. phys. Chem.* **219**, 699 (2005).
- <sup>21</sup>M. J. Frisch, G. W. Trucks, H. B. Schlegel *et al.*, GAUSSIAN 98, Rev. A.11.1, Gaussian, Inc., Pittsburgh, PA, 2001.
- <sup>22</sup>See EPAPS Document No. E-JCPA6-123-020529 for structural parameters, vibrational frequencies, and electronic energies of all intermediates and complexes. This document can be reached via a direct link in the online article's HTML reference section or via the EPAPS homepage (<http://www.aip.org/pubservs/epaps.html>).
- <sup>23</sup>O. K. Rice and H. C. Ramsperger, *J. Am. Chem. Soc.* **49**, 1617 (1927).
- <sup>24</sup>L. S. Kassel, *J. Phys. Chem.* **32**, 225 (1928).
- <sup>25</sup>R. A. Marcus and O. K. Rice, *J. Phys. Colloid Chem.* **55**, 894 (1951).
- <sup>26</sup>T. Baer and W. L. Hase, *Unimolecular Reaction Dynamics: Theory and Experiments* (Oxford University Press, New York, 1996).
- <sup>27</sup>P. K. Acharya, R. A. Kendall, and J. Simons, *J. Chem. Phys.* **83**, 3888 (1985).
- <sup>28</sup>H.-J. Werner, U. Mänz, and P. Rosmus, *J. Chem. Phys.* **87**, 2913 (1987).
- <sup>29</sup>Y. Li and J. M. Farrar, *J. Chem. Phys.* **120**, 199 (2004).
- <sup>30</sup>Y. Li and J. M. Farrar, *J. Phys. Chem. A* **108**, 9876 (2004).
- <sup>31</sup>J. O. Hirschfelder, *Int. J. Quantum Chem., Symp.* **3**, 17 (1969).
- <sup>32</sup>K. G. Anlauf, P. J. Kuntz, D. H. Maylotte, P. D. Pacey, and J. C. Polanyi, *Discuss. Faraday Soc.* **44**, 183 (1967).
- <sup>33</sup>K. G. Anlauf, J. C. Polanyi, W. H. Wong, and K. B. Woodall, *J. Chem. Phys.* **49**, 5189 (1968).
- <sup>34</sup>D. H. Maylotte, J. C. Polanyi, and K. B. Woodall, *J. Chem. Phys.* **57**, 1547 (1972).
- <sup>35</sup>C. A. Parr, J. C. Polanyi, and W. H. Wong, *J. Chem. Phys.* **58**, 5 (1973).
- <sup>36</sup>A. M. G. Ding, L. J. Kirsch, D. S. Perry, J. C. Polanyi, and J. L. Schreiber, *Faraday Discuss. Chem. Soc.* **55**, 252 (1973).
- <sup>37</sup>G. Herzberg, *Molecular Spectra and Molecular Structure*, 2nd ed. (Van Nostrand, Princeton, 1950).
- <sup>38</sup>W. B. Miller, S. A. Safron, and D. R. Herschbach, *Discuss. Faraday Soc.* **44**, 108 (1967).
- <sup>39</sup>M. K. Bullitt, C. H. Fisher, and J. L. Kinsey, *J. Chem. Phys.* **60**, 478 (1974).
- <sup>40</sup>S. Stolte, A. E. Proctor, and R. B. Bernstein, *J. Chem. Phys.* **65**, 4990 (1976).
- <sup>41</sup>S. T. Lee and J. M. Farrar, *J. Chem. Phys.* **113**, 581 (2000).
- <sup>42</sup>D. R. Herschbach, *Chem. Scr.* **27**, 327 (1987).
- <sup>43</sup>W. N. Olmstead and J. I. Brauman, *J. Am. Chem. Soc.* **99**, 4219 (1977).
- <sup>44</sup>M. J. Pellerite and J. I. Brauman, *J. Am. Chem. Soc.* **102**, 5993 (1980).